High Refractive Index Sensor for Tellurite Photonic Crystal Fiber Based on Soliton Self-Frequency Shift

Di Wu ⬤ , *Member, IEEE*, and Jing Zhang ⬤

Abstract—In this paper, a novel refractive index (RI) sensor based on the soliton self-frequency shift (SSFS) in tellurite photonic crystal fiber (TPCF) is proposed. RI sensing in the mid-infrared region is achieved by detecting the wavelength shift of the soliton. By exploiting the high RI property of the tellurite fiber, it is possible to measure surrogate liquids with higher RIs compared to conventional silica fibers. The sensitivity of the proposed sensor can reach up to 3657.5 nm/RIU when a fiber laser with a pulse width of 100 fs and pump wavelength (λ_P) of 2600 nm is used as the light source and a 1 m-long TPCF is utilized as the nonlinear medium. To the best of our knowledge, this is the first time that high RI sensing in the mid infrared region has been achieved by exploiting the SSFS effect in non-silica fibers such as TPCF.

Index Terms—High refractive index sensing, mid infrared, soliton self-frequency shift, tellurite photonic crystal fiber.

I. INTRODUCTION

REFRACTIVE index (RI) sensing is a technology that measures environmental characteristics by analyzing changes in the refractive index of a material [1], [2], [3]. The path of light and its speed are altered in a material based on its refractive index, which can be exploited to determine the environmental conditions to which the material is exposed, including concentration [8], [9], temperature [4], [5], pressure [6], [7], biomedical [10], [11], [12], and so on. The refractive index can be detected using several methods such as optical fiber interference [13], [14], diffraction gratings [15], [16], surface plasmon resonance [17], [18], and four-wave mixing [19], [20].

Tellurite photonic crystal fiber (TPCF) is widely used in the fiber optic sensing industry [21]. The TPCF can be used to fabricate refractive index sensors as it has a higher refractive index of up to 2.0 as compared to the quartz optical fiber, making it more suitable for detecting high refractive index liquids. Additionally, TPCF has good transmission in the mid-infrared band along with higher sensitivity. The TPCF also has high nonlinearity [22], [23], [24], [25], which can produce nonlinear effects such as four-wave mixing, self-phase modulation, and soliton generation.

Russell et al. [26] discovered that the soliton is a unique type of nonlinear light wave that possesses self-focusing, self-modulation, and stable transmission capabilities. This allows

it to be stably transmitted without attenuation over an extended distance in an optical fiber. Even when the waveform is distorted, it can retain its stability and preserve its amplitude and shape throughout transmission. For optical transmission in optical fibers, solitons are affected by Raman scattering, where the high-frequency component acts as a pump to transfer energy to the low-frequency component. This results in a constant shift of the central wavelength of the soliton towards longer wavelengths, known as the soliton self-frequency shift (SSFS) [27], [28], [29], [30], [31]. SSFS-based fiber optic sensors make use of the fact that the group velocity dispersion parameter and the nonlinear coefficient of an optical fiber vary with external factors when the phenomenon of soliton self-frequency shift occurs. This approach for achieving refractive index sensing offers great potential, although only a few studies have investigated this sensing modality.

In this paper, the design of a novel refractive index sensor is proposed that utilizes the SSFS effect in tellurite fibers. By taking advantage of the high refractive index property of tellurite fibers, surrogate liquids can be measured with higher refractive indices compared to traditional silica fibers. TeO_2-LiO_2-WO_3-MoO_3-Nb_2O_5 (TLWMN) glasses with distinct components form the core and cladding of the fiber, thereby enabling it to exhibit an RI of about 2.0. Consequently, the measurable refractive index range expands beyond that of silicon-based fibers, encompassing 1.65–1.73 range. Through simulations of SSFS, it is observed that the displacement of the soliton peak demonstrates a positive linear relationship with changes in RI. Notably, the sensitivity of the tellurite fiber RI sensor reaches a remarkable value of 3657.5 nm/RIU. Owing to its exceptional sensitivity, real-time performance, and non-destructive nature, the high refractive index sensing technology offered by tellurite fibers finds extensive applications in optical sensing and can be applied in other fields such as industrial automation, medical diagnostics, and environmental monitoring.

II. THE TPCF RI SENSOR MODEL

The core of the designed TPCF is a TLWMN with different components. The TPCF exhibits a significantly higher nonlinear index compared to conventional silica fiber, thus favoring soliton generation. Fig. 1 demonstrates the refractive index curves of the TLWMN glasses corresponding to each component.

The structure of the TPCF is illustrated in Fig. 2(a), where the core, the cladding, the four air holes filled with surrogate liquid, and the remaining air holes are represented by green,
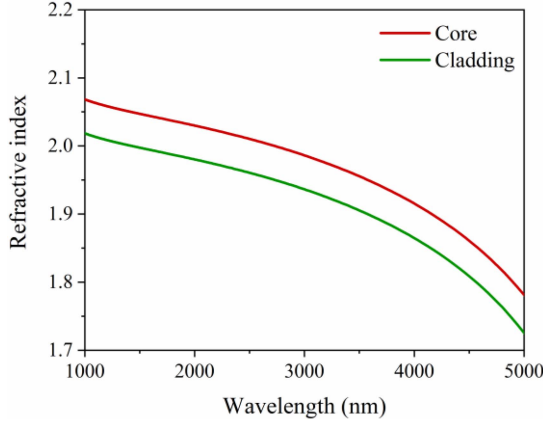
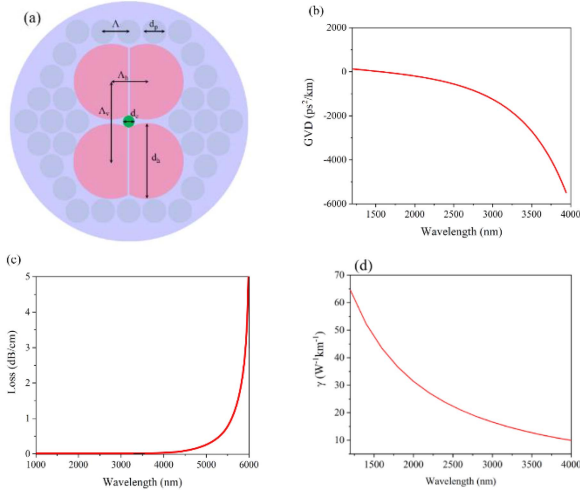Fig. 1. The refractive index curve of TLWMN Glasses.

Fig. 2. (a) The structure of TPCF; (b) dispersion of the optical fiber; (c) loss of the optical fiber; (d) nonlinear coefficient γ of the optical fiber.

Fig. 3. Demonstration diagram of SSFS sensing theory.

purple, pink, and gray colors, respectively. The group velocity dispersion (GVD) of the TPCF was determined for a refractive index of 1.65. Fig. 2(b) exhibits the GVD curve of the TPCF at RI = 1.65 calculated through the full vector finite element method employing the Lumerical Mode Solutions software package. The core diameter (d_c) of the TPCF, diameter of the four air holes filled with surrogate liquid (d_h), and the pore diameter (d_p) were 2.9 μm, 18.8 μm, and 6 μm, respectively. The vertical and horizontal distances between the four large holes, denoted by Λ_v and Λ_h, were 20 μm and 9 μm, respectively. The distance of the other holes, denoted by Λ was 6.5 μm.

Based on the parameters of the designed fiber structure, the zero-dispersion wavelength (ZDW) was calculated to be located near 1500 nm. It is beneficial to study the effect of SSFS with RI when the pump wavelength is located in the anomalous dispersion region, i.e., greater than the 1500 nm range. Fig. 2(c) shows the limiting loss calculated when there is no filling. It can be observed that the order of magnitude of the confinement loss is about 10^{-12} dB/cm in the range of the anomalous dispersion region, which has almost no effect on the production of solitons. Fig. 2(d) shows the nonlinear coefficient (γ) calculated at RI =
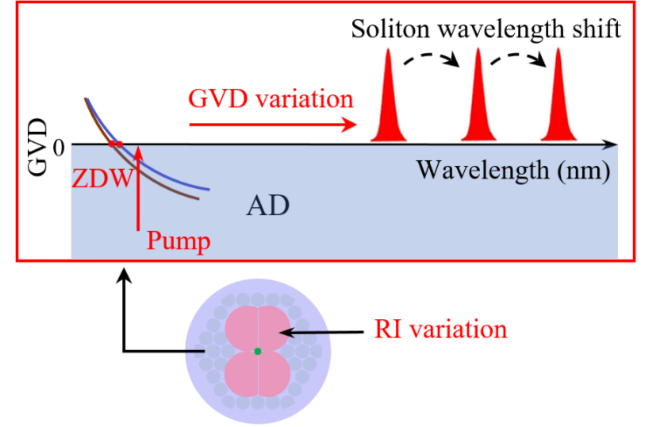
1.65, where γ varies from 64 to 10 $\mathrm{W^{-1}km^{-1}}$ in the 1200–4000 nm range, calculated as follows: $\gamma = \frac{n_2 \omega}{A_{eff} c} = \frac{2\pi n_2}{A_{eff} \lambda}$.

III. THEORETICAL ANALYSIS

When the RI changes, the GVD value of the TPCF also changes. This results in varying frequency shifts of the soliton generated by the Raman effect at different RIs, causing a wavelength shift of the soliton. In this paper, the conceptual implementation of sensing using SSFS is shown in Fig. 3. In order to study SSFS, the pulse transmission process is modeled in TPCF with the following expression. The optical soliton generation and temperature sensitivity properties in TPCF can be modelled by the generalized nonlinear Schrödinger equation (GNLSE) [32], [33], expressed as:

$$\frac{\partial A(z,t)}{\partial z} = -\frac{\alpha}{2} A(z,t) + \sum_{m \geq 2} \frac{i^{m+1}}{m!} \beta_m \frac{\partial^m A(z,t)}{\partial t^m}$$

$$+ i\gamma \left(1 + \frac{i}{\omega_0} \frac{\partial}{\partial t} \right) \times \left[A(z,t) \int_{-\infty}^{+\infty} R(t') |A(z, t-t')|^2 dt' \right] \quad (1)$$

where A(z, t) is the complex field envelope, z is the distance, α is the propagation loss, and β_m is the Taylor expansion coefficient of GVD.

The second term on the right-hand side of (1) is associated with dispersion, while the third term pertains to the nonlinear coefficient [34]. As the RI varies, these two terms also undergo changes. The principal factor contributing to the presence of Raman solitons is the Raman gain. The Raman gain coefficient serves as the paramount measure that characterizes the stimulated Raman scattering (SRS), and it can be defined as:

$$g_R(\Delta\omega) = \frac{\omega_0}{cn_0} f_R \chi^3 \mathrm{Im} \left[\tilde{h}_R(\Delta\omega) \right] \quad (2)$$

where Im denotes the imaginary part, $\Delta\omega = \omega - \omega_0$, c is the speed of light in vacuum, and f_R is the Raman contribution factor.

When the RI changes, the GVD and γ of the TPCF change, which causes changes in the second and third terms on the right side of the GNLSE. Therefore, as the RI changes, the wavelength of the soliton produced by the Raman effect changes, and sensing

TABLE I
PARAMETERS USED TO SIMULATE SSFS IN TPCF

P_0 (W)	W_0 (fs)	L (m)	γ (W^{-1}km^{-1})	α (dB/m)	λ_P (nm)
1000	100	1	Variation with RI	3	2200
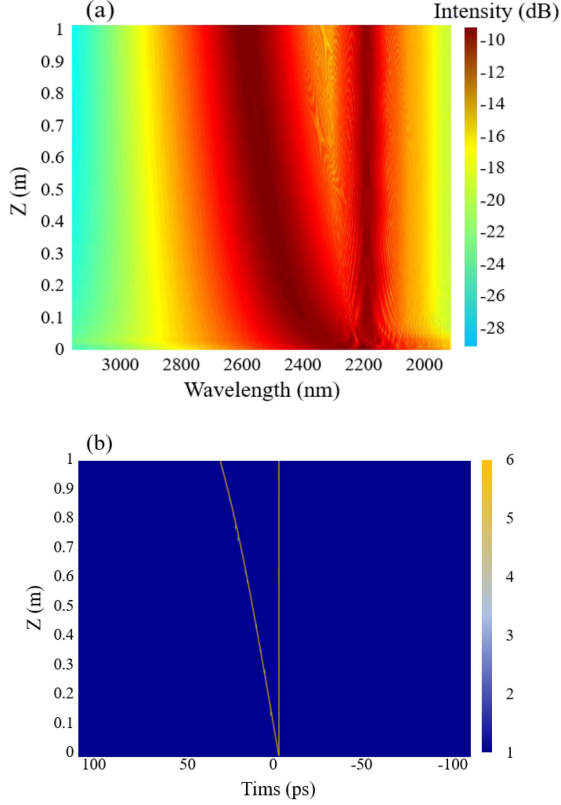
Fig. 4. The soliton evolution spectra in the (a) frequency and (b) time domains.
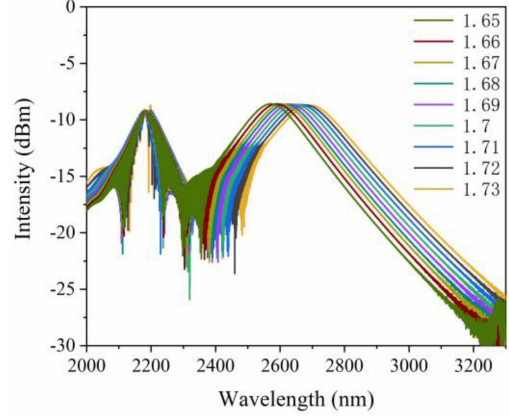

Fig. 5. Spectrogram of solitons at RI from 1.65 to 1.73.
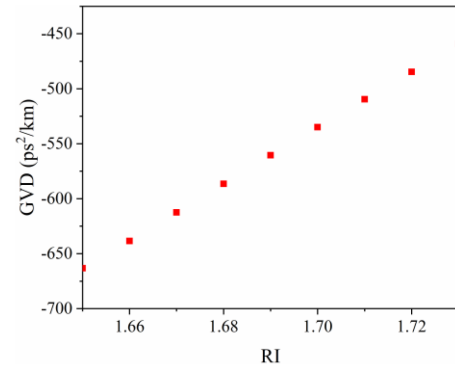
Fig. 6. The corresponding value of GVD with the RI changing from 1.65 to 1.73 at $\lambda_P = 2200$ nm.

can be achieved by observing the spectral changes. Herein, the peak wavelength value of the soliton is used as a monitoring criterion. The sensitivity S can be expressed as:

$$S = \frac{\Delta\lambda_{peak}}{\Delta n_a}(nm/RIU) \qquad (3)$$

where $\Delta\lambda_{peak}$ is the change in SSFS wavelength corresponding to the amount of change in refractive index of the analyte, and Δn_a is the amount of change in refractive index of the analyte.

IV. RESULTS AND DISCUSSION

To match the fiber dispersion profile and SSFS generation, the pump wavelength λ_P was set to 2200 nm. During the simulation, a fiber laser was utilized as the pump source with a pulse width (W_0) of 100 fs and a power (P_0) of 1000 W, and a 1 m long TPCF was used as the nonlinear medium. The nonlinear coefficient of the TPCF was calculated to be 27.2 W^{-1}km^{-1} at 2200 nm (Table I). The soliton evolution spectra in the frequency and time domains of 1 m TPCF at RI of 1.65 are shown in Fig. 4(a) and (b), respectively. The central wavelength of the fundamental soliton was about 2570 nm. Considering the refractive index of

the TPCF, the RI variations were selected from 1.65 to 1.73 in the calculations.

Varying the RI from 1.65 to 1.73 with $\lambda_P = 2200$ nm altered the GVD value of the TPCF, resulting in a wavelength shift of the soliton. The soliton motion was calculated at an RI interval of 0.01, as shown in Fig. 5. It can be observed that in the mid infrared region, the Raman soliton spectrum reaches a level of -8.3 dB, and the soliton wavelength redshifts from 2570 to 2693 nm.

It is important to note that the soliton moves in the long-wave direction as the RI increases. Using the perturbation method, the expression for the change in frequency due to the Raman effect when a soliton pulse is transmitted in an optical fiber can be derived as [35]:

$$\Delta\omega = -\frac{8W_R\gamma P_0 z}{15W_0^2} = -\frac{8W_R|\beta_2|z}{15W_0^4} \qquad (4)$$

Here, the WR originates from the Raman delay response with the condition $N = \gamma P_0 W_0^2/|\beta_2| = 1$, where N is the soliton order and N = 1 denotes the fundamental soliton. A negative sign indicates a decrease in carrier frequency, i.e., the soliton spectrum is shifted to a longer wavelength. If WR is assumed to be constant at the same pump wavelength, $\Delta\omega$ will be proportional to the absolute value of $|\beta_2|$ (GVD value). From Fig. 6, it can be observed that $|\beta_2|$ decreases as the RI increases from
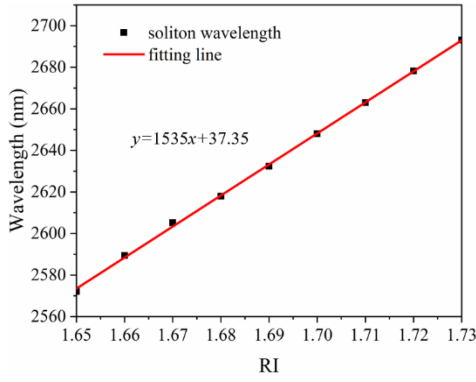
Fig. 7. The fitting line of the soliton peak movement with the RI variation at $\lambda_P = 2200$ nm.
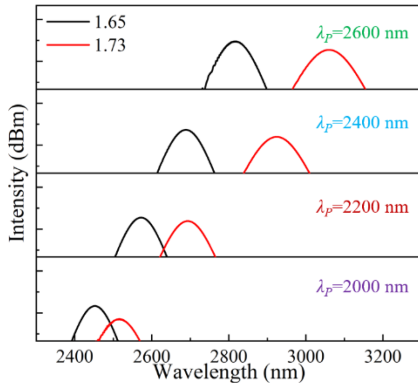

Fig. 9. The fitting line of the soliton peak movement with the RI variation at different λ_P: green for 2000 nm, purple for 2200 nm, red for 2400 nm, and blue for 2600 nm.

Fig. 8. Theoretical soliton wavelength shift spectra with the variation of λ_P at 1.65 and 1.73.

1.65 to 1.73, resulting in a decrease in the frequency shift of the soliton. This is evident from the shift of the soliton wavelength towards longer wavelengths in the spectrum.

Fig. 7 shows the RI as a function of the soliton wavelength as it varies from 1.65 to 1.73 at $\lambda_P = 2200$ nm. The isolated wave peak obtained from Fig. 5(b) has a good linear relationship with ΔRI. Therefore, the variation of the soliton wavelength caused by the change of RI can be used as RI sensing. The peak of Raman soliton spectrum is 2570 nm when RI is 1.65 and 2693 nm when RI is 1.73. The theoretical sensitivity of TPCF is determined to be 1535 nm/RIU. In order to obtain a higher sensitivity, a detailed displacement of the soliton wavelengths was carried out with the change of RI at different λ_P and different P_0 studies, as shown below.

A. Shift of Soliton Wavelength With Different λ_P

The spectra of the soliton wavelength with RI were simulated at 2000 nm, 2400 nm, and 2600 nm, and compared with $\lambda_P = 2200$ nm. The lengths of P_0, W_0, and TPCF were kept constant. Due to the strong linear relationship between ΔRI and the soliton peak, only the spectra at RI of 1.65 and 1.73 were simulated, as shown in Fig. 8. The corresponding peak shifts of the soliton wavelength-shifted spectra are shown in Fig. 9, where the temperature sensitivity of the TPCF can be observed to be 780 nm/RIU, 1535 nm/RIU, 2932.5 nm/RIU, and 3035
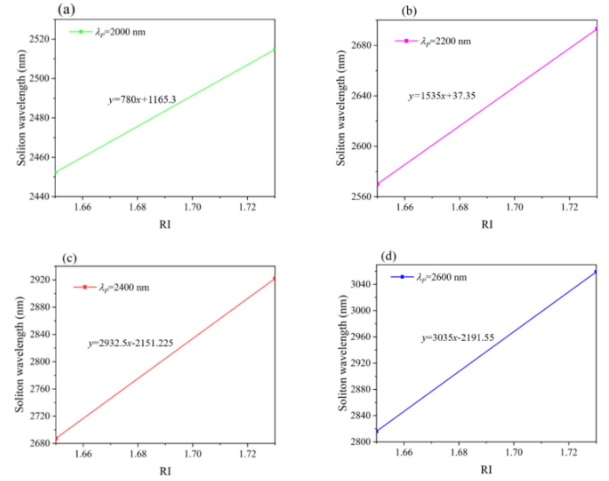
nm/RIU at the pump center wavelengths of 2000 nm, 2200 nm, 2400 nm and 2600 nm, respectively.

It is evident that higher sensitivity is obtained by pumping at 2600 nm when only λ_P is changed. In addition, the sensitivity of TPCF is enhanced as the wavelength of the pump center is increased. According to (7), $\Delta\omega$ is proportional to $|\beta_2|$. $\Delta\omega_2$ and $\Delta\omega_1$ refer to the frequency shifts at RI of 1.65 and 1.73, respectively, and β_2 and β'_2 are the GVD values at RI of 1.65 and 1.73, respectively. The frequency shift difference between the two generated isolated waves is given by:

$$\Delta\omega_2 - \Delta\omega_1 = -\left[\frac{8W_R\,|\beta_2|\,z}{15W_0^4} - \frac{8W_R\,|\beta'_2|\,z}{15W_0^4}\right]$$
$$= \frac{8W_R z\,[|\beta_2| - |\beta'_2|]}{15W_0^4} \quad (5)$$

Equation (5) clearly shows that the frequency shift difference is related to$|\beta_2|$-$|\beta'_2|$. The GVD value β_2 is calculated at different pump center wavelengths with RI from 1.65 and 1.73, as shown in Fig. 8. It can be observed that as RI increases, β_2 decreases $||\beta_2|$-$|\beta'_2||$>0. At 2600 nm, the difference in $|\beta_2|$ is the largest, and thus the frequency shift difference in the SSFS spectra will be the largest, which in turn will result in the highest sensitivity, corresponding to results shown in Fig. 9.

B. Shift of Soliton Wavelength With Different P_0

The shift of the soliton wavelength was calculated with respect to the variation of P_0 to detect the sensitivity of the TPCF sensor when λ_P was fixed at 2600 nm, $L = 1$ m, and $W_0 = 100$ fs. P_0 was tuned to 800 W, 1000 W, 1200 W, 1400 W, and 1600 W.

Fig. 10 shows the shift of soliton wavelength with respect to the variation of P_0 at RIs of 1.65 and 1.73 when L and W_0 are constant and $\lambda_P = 2600$ nm. The soliton wavelength was redshifted with increasing P_0 and the $\Delta\omega$ also increased. Fig. 11 shows the fitted curves corresponding to the peak shift of the soliton for different P_0 in Fig. 10. The sensitivity of the TPCF sensors is also shown in Fig. 11. It can be seen that the highest
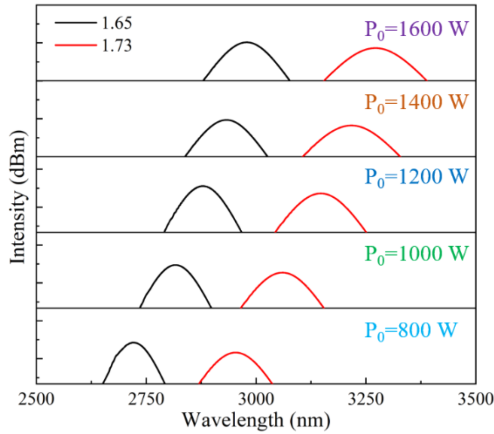
Fig. 10. Theoretical soliton wavelength shift spectra with the variation of P_0 at 1.65 and 1.73.
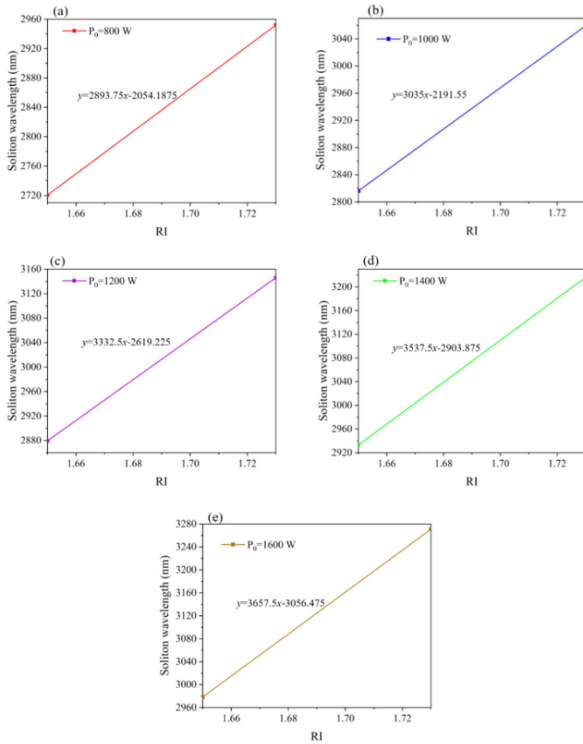

Fig. 11. The fitting line of the soliton peak movement with the RI variation at different P_0: red for 800 W, blue for 1000 W, purple for 1200 W, green for 1400 W, and brown for 1600 W.

sensitivity of the TPCF RI sensor was up to 3207.5 nm/RIU at λ_P of 2600 nm and P_0 of 1600 W.

Figs. 9 and 11 demonstrate that the sensitivity of the sensor changes as the pump wavelength and input power change. To obtain the highest sensor sensitivity, the λ_P was chosen to be 2600 nm and P_0 was 1600 W.

V. CONCLUSION

This paper investigates the variation of soliton wavelength with RI for different pumping wavelengths and powers. The SSFS effect was simulated, and it was observed that the displacement of the soliton peak demonstrated a strong linear

relationship with the change of RI. The proposed tellurite photonic crystal fiber (TPCF) RI sensor achieved a remarkable sensitivity of up to 3207.5 nm/RIU at a pumping wavelength (λ_P) of 2600 nm and power (P_0) of 1600 W. To the best of our knowledge, this is the first application of TPCF in mid-infrared RI sensing, capable of measuring RI in the range of 1.65-1.73, which cannot be achieved by conventional quartz fiber optic sensors. This research opens up new possibilities in the field of RI sensors and provides a new direction for future studies. The ongoing advancements in optical technology have led to continuous innovation and improvement in RI sensing, making it a valuable tool in several fields. We anticipate that the continued development of this sensing technology will offer even higher sensitivity and a broader range of applications in the field of optical sensing.

V. DECLARATION OF INTERESTS

The authors declare that they have no known competing financial interests or personal relationships that could have appeared to influence the work reported in this paper.

REFERENCES

[1] M. White Ian and X. Fan, "On the performance quantification of resonant refractive index sensors," *Opt. Exp.*, vol. 16, no. 2, pp. 1020–1028, Jan. 2008.

[2] T. Wei et al., "Temperature-insensitive miniaturized fiber inline fabry-perot interferometer for highly sensitive refractive index measurement," *Opt. Exp.*, vol. 16, no. 8, pp. 5764–5769, Apr. 2008.

[3] S. Bandyopadhyay, T. K. Dey, N. Basumallick, P. Biswas, K. Dasgupta, and S. Bandyopadhyay, "High sensitive refractometric sensor using symmetric cladding modes of an FBG operating at mode transition," *J. Lightw. Technol.*, vol. 34, no. 14, pp. 3348–3353, Jul. 2016.

[4] T. Cheng et al., "Numerical demonstration of mid-infrared temperature sensing by soliton self-frequency shift in a fluorotellurite microstructured fiber," *Appl. Phys. B*, vol. 127, no. 12, pp. 1–11, Dec. 2021.

[5] Y. Xue et al., "Ultrasensitive temperature sensor based on an isopropanol-sealed optical microfiber taper," *Opt. Lett.*, vol. 38, no. 8, pp. 1209–12011, Apr. 2013.

[6] Y. Zhang et al., "A high-sensitivity fiber grating pressure sensor and its pressure sensing characteristics," *Acta Optica Sinica*, vol. 22, no. 1, pp. 89–91, 2002.

[7] U. Biswas et al., "Modeling and analysis of all-optical pressure sensor using photonic crystal based micro ring resonator," *Int. J. Numer. Modelling Electron. Netw. Devices Fields*, vol. 35, no. 2, Mar. 2022, Art. no. e2962.

[8] M. Castillo et al., "Optical sensor technology for measuring whey fat concentration in cheese making," *J. Food Eng.*, vol. 71, no. 4, pp. 354–360, Dec. 2005.

[9] N. Ozana et al., "Improved noncontact optical sensor for detection of glucose concentration and indication of dehydration level," *Biomed. Opt. Exp.*, vol. 5, no. 6, pp. 1926–1940, Jun. 2014.

[10] Z. Chen et al., "A CRISPR/cas12a-empowered surface plasmon resonance platform for rapid and specific diagnosis of the omicron variant of SARS-COV-2," *Nat. Sci. Rev.*, vol. 9, no. 8, pp. 100–109, Jun. 2022.

[11] T. Xue et al., "Ultrasensitive detection of miRNA with an antimonene-based surface plasmon resonance sensor," *Nature Commun.*, vol. 10, Jan. 2019, Art. no. 28.

[12] F. Zheng et al., "A highly sensitive CRISPR-empowered surface plasmon resonance sensor for diagnosis of inherited diseases with femtomolar-level real-time quantification," *Adv. Sci.*, vol. 9, no. 14, May 2022, Art. no. 2105231.

[13] L. Xu, Y. Li, and B. Li, "Nonadiabatic fiber taper-based mach-zehnder interferometer for refractive index sensing," *Appl. Phys. Lett.*, vol. 101, no. 15, Oct. 2012, Art. no. 153510.

[14] B. Yang et al., "Balloon-like singlemode-tapered multimode-singlemode fiber structure for refractive index sensing," *Proc. SPIE*, vol. 10464, 2017, Art. no. 104641E.

[15] G. Li et al., "Double-layered metal grating for high-performance refractive index sensing," *Opt. Exp.*, vol. 23, no. 7, pp. 8995–9003, Apr. 2015.

[16] Y. Xu et al., "Wide-range refractive index sensing relied on tracking the envelope spectrum of a dispersive subwavelength grating microring resonator," *Opt. Laser Technol.*, vol. 154, Oct. 2022, Art. no. 108304.

[17] T. Huang, "Highly sensitive SPR sensor based on D-shaped photonic crystal fiber coated with indium tin oxide at near-infrared wavelength," *Plasmonics*, vol. 12, no. 3, pp. 1–6, Jun. 2016.

[18] A. Akouibaa, A. Akouibaa, and R. Masrour, "Numerical study of a D-shaped optical fiber SPR biosensor for monitoring refractive index variations in biological tissue via a thin layer of gold coated with titanium dioxide," *Spectrochimica Acta Part A: Mol. Biomol. Spectrosc.*, vol. 304, Jan. 2024, Art. no. 123358.

[19] Y. Gao et al., "A refractive index sensor based on four wave mixing in d shaped tellurite photonic crysta1 fiber," *Photon. Sensors*, vol. 13, no. 3, Sep. 2023, Art. no. 230312.

[20] Y. Sun et al., "Theoretical investigation of an alcohol-filled tellurite photonic crystal fiber temperature sensor based on four-wave mixing," *Sensors*, vol. 20, no. 4, Feb. 2020, Art. no. 1007.

[21] J. Wang, E. M. Vogel, and E. Snitzer, "Tellurite glass: A new candidate for fiber devices," *Opt. Mater.*, vol. 13, no. 3, pp. 187–203, Dec. 1994.

[22] J. Yuan et al., "Efficient and broadband Stokes wave generation by degenerate four-wave mixing at the mid-infrared wavelength in a silica photonic crystal fiber," *Opt. Lett.*, vol. 38, no. 24, pp. 5288–5291, Dec. 2013.

[23] J. Yuan et al., "Enhanced intermodal four-wave mixing for visible and near-infrared wavelength generation in a photonic crystal fiber," *Opt. Lett.*, vol. 40, no. 7, pp. 1338–1341, Apr. 2015.

[24] Y. Geng et al., "Wavelength multiplexing of four-wave mixing based fiber temperature sensor with oil-filled photonic crystal fiber," *Opt. Exp.*, vol. 26, no. 21, pp. 27907–27916, Oct. 2018.

[25] Y. Geng, L. Wang, X. Tan, Y. Xu, X. Hong, and X. Li, "A compact four-wave mixing-based temperature fiber sensor with partially filled photonic crystal fiber," *IEEE Sens. J.*, vol. 19, no. 8, pp. 2956–2961, Apr. 2019.

[26] J. S. Russell, "Report on Waves," Report of the 14th Meeting of the British Association for the Advancement of Science, pp. 311–390, 1844.

[27] F. Mitschke and L. F. Mollenauer, "Discovery of the soliton self-frequency shift," *Opt. Lett.*, vol. 11, no. 10, pp. 659–661, 1986.

[28] J. P. Gordon, "Theory of the soliton self-frequency shift," *Opt. Lett.*, vol. 11, no. 10, pp. 662–664, 1986.

[29] J. Santhanam and G. P. Agrawal, "Raman-induced spectral shifts inoptical fibers: General theory based on the moment method," *Opt.Commun.*, vol. 222, no. 1, pp. 413–420, Jul. 2003.

[30] J. H. Lee, J. van Howe, C. Xu, and X. Liu, "Soliton self-frequency shift: Experimental demonstrations and applications," *IEEE J. Sel. Topics Quantum Electron.*, vol. 14, no. 3, pp. 713–723, May/Jun. 2008.

[31] A. A. Voronin and A. M. Zheltikov, "Soliton self-frequency shift decelerated by self-steepening," *Opt. Lett.*, vol. 33, no. 15, pp. 1723–1725, Aug. 2008.

[32] Y. L. Chou et al., "A novel optical fiber temperature sensor with polymer-metal alternating structure," *Opt. Laser Technol.*, vol. 115, pp. 186–192, Jul. 2019.

[33] F. Wang et al., "Numerical demonstration of widely tunable femtosecond soliton generation in chalcogenide microstructured fibers," *Laser Phys. Lett.*, vol. 16, no. 10, Oct. 2019, Art. no. 105402.

[34] X. Zhou et al., "High-sensitivity SPR temperature sensor based on hollow-core fiber," *IEEE Trans. Instrum. Meas.*, vol. 69, no. 10, pp. 8494–8499, Oct. 2020.

[35] G. P. Agrawal, *Nonlinear Fiber Optics*. San Diego, CA, USA: Academic, 2009.